HHS Public Access

Author manuscript

J Am Chem Soc. Author manuscript; available in PMC 2016 December 16.

Published in final edited form as:

J Am Chem Soc. 2015 December 16; 137(49): 15548–15557. doi:10.1021/jacs.5b10748.

A Manganese Alternative to Gadolinium for MRI Contrast

Eric M. Gale[*], **Iliyana P. Atanasova**, **Francesco Blasi**, **Ilknur Ay**, and **Peter Caravan**[*]

The Athinoula A. Martinos Center for Biomedical Imaging, The Institute for Innovation in Imaging, Department of Radiology, Massachusetts General Hospital, Harvard Medical School, 149 Thirteenth Street, Suite 2301, Charlestown, Massachusetts 02129

Abstract

Contrast-enhanced computed tomography (CT) and magnetic resonance imaging (MRI) are routinely used to diagnose soft tissue and vascular abnormalities. However safety concerns limit the use of iodinated and gadolinium- (Gd) based CT and MRI contrast media in renally compromised patients. With an estimated 14% of the US population suffering from chronic kidney disease (CKD), contrast media compatible with renal impairment is sorely needed. We present the new manganese(II) complex $[Mn(PyC3A)(H_2O)]^-$ as a Gd alternative. $[Mn(PyC3A)(H_2O)]^-$ is amongst the most stable Mn(II) complexes at pH 7.4 (log K_{ML} = 11.40). In the presence of 25 mol equiv. Zn at pH 6.0, 37 °C, $[Mn(PyC3A)(H_2O)]^-$ is 20-fold more resistant to dissociation than $[Gd(DTPA)(H_2O)]^{2-}$. Relaxivity of $[Mn(PyC3A)(H_2O)]^-$ in blood plasma is comparable to commercial Gd contrast agents. Biodistribution analysis confirms that $[Mn(PyC3A)(H_2O)]^-$ clears via a mixed renal/ hepatobiliary pathway with >99% elimination by 24h. $[Mn(PyC3A)(H_2O)]^-$ was modified to form a bifunctional chelator and 4 chelates were conjugated to a fibrin-specific peptide to give Mn-FBP. Mn-FBP binds the soluble fibrin fragment DD(E) with K_d = 110 nM. Per Mn relaxivity of Mn-FBP is 4-fold greater than $[Mn(PyC3A)(H_2O)]^-$ and increases 60% in the presence of fibrin, consistent with binding. Mn-FBP provided equivalent thrombus enhancement to the state of the art Gd analog, EP-2104R, in a rat model of arterial thrombosis. Mn metabolite analysis reveals no evidence of dechelation and the probe was >99% eliminated after 24 hr. $[Mn(PyC3A)(H_2O)]^-$ is a lead development candidate for an imaging probe that is compatible with renally compromised patients.

Introduction

Chronic kidney disease (CKD) affects 14% of the US adult population, and this prevalence is increasing with the epidemic of diabetes.[1] CKD is characterized by progressive deterioration of renal function (staged 1-5 by glomerular filtration rate (GFR)) that culminates in kidney failure. Poor kidney function is often associated with other co-

[*]Corresponding Authors: egale@nmr.mgh.harvard.edu, caravan@nmr.mgh.harvard.edu.

Author Contributions: The manuscript was written through contributions of all authors. / All authors have given approval to the final version of the manuscript.

Associated Content: Supporting Information. Experimental details, synthetic procedures, compound characterization, structures of molecules not depicted in main text, pH-dependent speciation of $[Mn(PyC3A)(H_2O]^-$, thermodynamic, kinetic, relaxivity and water exchange paramaters of Mn and Gd complexes, additional MR images, bio-distribution data and LC-ICP-MS traces. This material is available free of charge via the Internet at http://pubs.acs.org.

morbidities. For instance, 86% of patients with stage 4 CKD suffer at least one co-morbidity.[2] Along with diabetes, the most commonly experienced co-morbidities are cardiovascular disease and hypertension, as many facets of cardiovascular physiology are intimately linked to kidney function.[2-4] This is a patient population that will benefit from contrast-enhanced computed tomography (CT) or magnetic resonance imaging (MRI) to detect disease, to monitor disease progression, and to guide therapeutic decisions. Because CKD is so prevalent, these patients may also require imaging for other pathologies unassociated with CKD, e.g. malignancies.

Unfortunately, routinely ordered contrast enhanced imaging protocols are incompatible with renal compromise. For the estimated 7.7% of US adults experiencing moderate to severe CKD (stage 3 and higher),[5] the iodinated contrast media used to delineate vascular and soft tissue structures in CT scans carries the risk of a severe and sometimes irreversible loss of renal function termed contrast induced nephropathy (CIN).[6,7] Gadolinium- (Gd) based imaging probes used in contrast-enhanced MRI are linked to the onset of nephrogenic systemic fibrosis (NSF), a rare but severe and potentially fatal fibrosis of the skin and internal organs that can arise in renally impaired patients.[8,9] The risk of both CIN and NSF increases with decreasing GFR. Iodinated radiocontrast and 3 Gd-based MR probes comprised of acyclic chelates are contraindicated for patients staged CKD ≥ 3.[6,7,10] It is worth noting that macrocycle based Gd-imaging probes exhibit superior stability and inertness relative to the acyclic probes and there are few unconfounded accounts linking NSF to macrocycle based Gd probes. Despite this fact, all Gd-based probes come with an FDA black box warning and American College of Radiology guidelines advise against the use of any Gd in patients suffering acute kidney injury or with GFR <40 mL/min/1.73m^2.[11] As a result, patients are often not imaged and clinicians must make management decisions with limited diagnostic information.[12] More recently, a number of reports have identified dose dependent Gd accumulation in the brains of patients with normal renal function that have received contrast enhanced MRI,[13-18] raising further concerns by the FDA regarding this class of compounds. Gadolinium retention in a subset of patients further underscores the need for Gd-free alternatives to enhance MR contrast.

The development of safe alternative imaging probes that are compatible with renal insufficiency stands to profoundly impact patient outcomes within a large and challenging population. The ideal probe would be amenable to as broad of a range of imaging applications as the routinely used iodinated CT contrast and Gd-based MR probes. The probe should freely distribute in the blood and in the extravascular, extracellular space and then clear rapidly. At least partial non-renal excretion must occur to circumvent the clearance barrier imposed by renal compromise. The probe should also enhance image contrast with sensitivity comparable to or better than currently used imaging probes.

Several classes of imaging probes have been considered as alternatives but all have drawbacks. Nanoparticles, e.g. iron oxides, generate superb MR image contrast but their large size limits their use to angiography, liver imaging, and niche applications targeting macrophages.[19] Furthermore, the adverse effect profile of nanoparticles is troubling. Ferumoxytol is associated with severe anaphylaxis and at least 18 patients deaths and now also carries an FDA black box warning.[20] MR imaging probes that provide contrast via

chemical exchange saturation or direct detection of NMR active nuclei require at least an order of magnitude higher doses compared to Gd-based probes.[21] Nuclear medicine techniques such as single photon emission computed tomography (SPECT) and positron emission tomography (PET) are highly sensitive but do not provide spatial resolution sufficient to delineate many vascular and tissue abnormalities.[22]

Manganese- (Mn) based complexes have also been considered as Gd-alternatives. The Mn^{2+} ion exhibits all of the physical properties that make Gd^{3+} a highly efficient imaging probe in T_1-weighted MR protocols: both ions are characterized by high spin quantum number (S = 7/2 for Gd^{3+}, S = 5/2 for Mn^{2+}), long longitudinal electronic relaxation times, and fast water exchange kinetics.[22,23] Mn is biogenic, and intravenously administered Mn^{2+} is cleared via biliary excretion, a particularly attractive feature in the context of renal compromise. Indeed, the complex $[Mn(DPDP)]^{3-}$ (Figure S6) was approved for use as a liver imaging agent.[24,25] It was shown that $[Mn(DPDP)]^{3-}$ undergoes partial dechelation in plasma and the Mn^{2+} ion is then rapidly taken up by hepatocytes, pancreatic tissue and cardiomyocytes.[26,27] $[Mn(DPDP)]^{3-}$ highlights both the promise and challenge of using Mn^{2+}. On the one hand $[Mn(DPDP)]^{3-}$ generated exquisite image contrast demonstrating the efficacy of a Mn-based approach, on the other hand $[Mn(DPDP)]^{3-}$ highlights the extreme lability of the Mn^{2+} ion and the challenge of designing a stable Mn-chelate.

We set out to rationally design chelators that afford stable Mn^{2+} complexes suitable for the same MR imaging applications as Gd-based probes: small, hydrophilic complexes useful for angiography,[28,29] lesion identification,[30,31] and characterization of tissue perfusion,[32] as well as bifunctional Mn^{2+} chelators that can be used in molecular MR applications. Here we introduce a new chelator PyC3A that forms a stable, inert complex with Mn^{2+} and provides equivalent relaxivity to Gd-based chelates used clinically. A bifunctional version of PyC3A enables the development of targeted probes and here we demonstrate a fibrin-targeted Mn-based probe for molecular imaging of thrombosis. We first characterized the thermodynamic stability, kinetic inertness with respect to transmetallation, relaxivity, hydration state, and water exchange kinetics of the Mn-complexes. For the fibrin-targeted probe we characterized its fibrin binding properties and relaxivity, and then compared it to a known Gd-based fibrin probe with MR imaging in a rat model of thrombosis. Detailed pharmacokinetic and biodistribution studies were performed to establish the in vivo stability of the Mn-chelate, and to show that it is completely excreted.

Results

Design and synthesis of Mn-based imaging probe

We outlined several design criteria at the outset of this work to address safety and efficacy. First, we aimed to maximize the thermodynamic stability of the Mn-chelate. Equally important, the chelate must be inert to Mn^{2+} dissociation. High T_1-relaxivity ($r_1 = \Delta(1/T_1)/[Mn]$) is another requisite. In order to achieve high relaxivity there must be a water co-ligand that undergoes relaxation and rapid exchange with bulk solvent.[23,35] The imaging probe should be hydrophilic and anionic to promote both high solubility for formulation as well as a likely extracellular distribution. We also sought a modest degree of lipophilicity to promote at least partial biliary clearance. Finally, the chelator should also be readily

amenable to synthetic modulation for further optimization or bio-conjugation. The Mn^{2+} chelator *N*-picolyl-*N*,*N*′,*N*′-*trans*-1,2-cyclohexylenediaminetriacetate (PyC3A, Scheme 1) meets these criteria. A survey of the coordination chemistry literature reveals that at pH 7.4 the most stable Mn^{2+} complexes are formed from polyaminocarboxylate ligands (Figure S6, Table S1). Hexadenate, acyclic ligands such as EDTA tend towards ternary, hepta-coordinate Mn^{2+} complexes with a labile water co-ligand, which provide suitable relaxivity.[34,36-38] On the other hand the most stable Mn^{2+} macrocyclic complexes have no water co-ligand.[39] We know from prior experience with Mn^{2+} complexes of the ligand HBET and various derivatives (Figure S6) that replacement of a single acetate-*O* donor with a different donor group results in complexes of comparable stability without precluding coordination of a water co-ligand.[34]

The *trans*-1,2-cyclohexylene linkage and pyridyl-*N* donor were incorporated within the chelate backbone to promote kinetic inertness with respect to Mn^{2+} dissociation. The propensity of the *trans*-1,2-diaminocyclohexane backbone to promote kinetic inertness is well documented, and has been shown to decrease the Mn^{2+} dissociation rate in the presence of competing metal ions by 4 orders of magnitude compared to an ethylene backbone.[33] The pyridyl-*N* donor was incorporated with the aims of further rigidifying the chelate, adding additional lipophilic character to the chelate, and to add an achiral point of synthetic elaboration for molecular imaging applications. Prior NMR studies have demonstrated that metal complexes of acyclic pyridyl-*N* containing chelates exhibit a lesser degree of fluxionality in solution than those formed by analogous chelates featuring acetate-*O* donors instead.[40] We rationalized that this effect will boost kinetic inertness. We also rationalized that the *trans*-1,2-cyclohexanediamine linkage and pyridyl-*N* donor combine could provide sufficient lipophilic character to promote hepatic uptake, and thus partial non-renal clearance of the resultant anionic Mn complex. The pyridyl-N group is highly modular and provides easy access to bifunctional derivatives for bioconjugation and molecular imaging.

PyC3A is prepared in 5 steps (Scheme 1). Mono-benzylation of *trans*-1,2-diaminocyclohexane followed by exhaustive alkylation with ^{t}butyl bromoacetate, then benzyl deprotection via hydrogenation over Pd/C yields *N*,*N*,*N*′-*trans*-1,2-cyclohexylenediaminetri-^{t}butylacetate (**3**), a synthon common to both PyC3A and its bi-functional derivative (see below). Reaction of **3** with picolyl chloride followed by removal of the ^{t}Bu protecting groups in neat TFA yields PyC3A, isolated as PyC3A•TFA. $[Mn(PyC3A)(H_2O)]^-$ was prepared by mixing the ligand with 1 mol equiv. $MnCl_2$ in water and adjusting the pH to 6.5.

Physicochemical evaluation of $[Mn(PyC3A)(H_2O)]^-$

$[Mn(PyC3A)(H_2O)]^-$ is amongst the most thermodynamically stable Mn^{2+} complexes reported (Table S1). Ligand protonation constants and Mn^{2+} thermodynamic stability constants in 0.15 M NaCl, 25 °C, were determined by pH-potentiometry (Table 1). The thermodynamic stability constant at pH 7.4 was also measured through direct competition with CDTA monitored using LC-MS (Figure S9). Potentiometric titration (Figure 1A) yields a stability constant log K = 14.14, and a conditional stability constant log $K_{pH\ 7.4}$ = 11.34 which is in excellent agreement with log $K_{pH\ 7.4}$ = 11.40 calculated from the CDTA

challenge. Figure S10 depicts Mn^{2+} composition as a function of pH in a solution containing 1 mM each Mn^{2+} and PyC3A, 0.15M NaCl, 25 °C and demonstrates that complexation is complete by pH 4.5.

$[Mn(PyC3A)(H_2O)]^-$ is also very inert to Mn^{2+} transmetallation. We stressed the complex under two sets of extreme conditions and compared the rates of metal ion displacement to other stable Mn^{2+} and Gd^{3+} complexes. Kinetic inertness was evaluated by challenging $[Mn(PyC3A)(H_2O)]^-$ with 25 mol. equiv. Zn^{2+} at pH 6.0, 37 °C, and using relaxivity as a readout. The transmetallation kinetics of $[Mn(CDTA)(H_2O)]^{2-}$ and $[Gd(DTPA)(H_2O)]^{2-}$ were measured as comparative benchmarks. Of previously reported Mn^{2+} complexes, $[Mn(CDTA)(H_2O)]^{2-}$ is the most kinetically inert system that allows direct Mn^{2+}-water interaction and thus sufficient relaxivity.[33] $[Gd(DTPA)(H_2O)]^{2-}$ is the active ingredient in Magnevist, the most widely used clinical MR contrast agent. Mn^{2+} displacement was recorded by measuring solvent T_2 as a function of time, as r_2 of free Mn^{2+} is ∼30-fold that of the chelated, monohydrated ion (Figure 1B),[41] Gd^{3+} displacement was measured via monitoring T_1 change. These experimental conditions allowed for homogenous reaction mixtures and rapid data acquisition.

$[Mn(PyC3A)(H_2O)]^-$ was 2-fold more inert to Zn^{2+} challenge than $[Mn(CDTA)(H_2O)]^{2-}$ and 20-fold more inert than $[Gd(DTPA)(H_2O)]^{2-}$. Pseudo-first order rate constants were $6.76\pm0.03 \times 10^{-4}$, $1.10\pm0.01 \times 10^{-3}$ and $1.41\pm0.31 \times 10^{-2}$ s^{-1} for $[Mn(PyC3A)(H_2O)]^-$, $[Mn(CDTA)(H_2O)]^{2-}$ and $[Gd(DTPA)(H_2O)]^{2-}$, respectively. Prior accounts characterizing Mn^{2+} transmetallation using various chelates including CDTA indicate spontaneous MLH dissociation as the predominant pathway,[33,39,42-45] and $[Mn(PyC3A)(H_2O)]^-$ transmetallation likely proceeds through an analogous mechanism. We expect the relative inertness observed at pH 6 to remain constant across the range of pH potentially encountered in vivo. We also evaluated $[Mn(PyC3A)(H_2O)]^-$ under a standard set of conditions used to comparatively evaluate the inertness of Gd complexes, i.e. challenge with Zn^{2+} and phosphate ion at pH 7 (Figures S11-12). Under these conditions, $[Mn(PyC3A)(H_2O)]^-$ showed similar inertness to approved acyclic Gd-based contrast agent $[Gd(DTPA)(H_2O)]^{2-}$.

The temperature dependence of bulk water ^{17}O T_2 (Figure 1C) demonstrates that an inner-sphere water co-ligand is present in $[Mn(PyC3A)(H_2O)]^-$, and that this water under goes very fast exchange with solvent.[46,47] The water exchange rate at 37 °C for $[Mn(PyC3A)(H_2O)]^-$ is $k_{ex} = 1.0 \times 10^8$ s^{-1}; associated kinetic parameters are listed in Table 2.

The relaxivity of $[Mn(PyC3A)(H_2O)]^-$ in blood plasma is equivalent to clinical Gd-based contrast agents such as $[Gd(DTPA)(H_2O)]^{2-}$ (Figures 1D and S8, Table S3). Relaxivity measurements were performed at 1.4 T, 37 °C. Relaxivity was 2.1 $mM^{-1}s^{-1}$ in pH 7.4 buffer and increased to 3.8 $mM^{-1}s^{-1}$ in bovine blood plasma, similar to Gd-DTPA and Gd-DOTA (4.1 and 3.6 $mM^{-1}s^{-1}$ in plasma).[48] The near doubling in r_1 observed in plasma is attributed to low-affinity interactions with serum proteins, which increases relaxivity at 1.4T.[23,35,37,41] Indeed, similar r_1 (3.4 $mM^{-1}s^{-1}$) is measured in 4.5% w/v BSA solution. Weak protein binding was confirmed by measurement of the fraction of protein bound $[Mn(PyC3A)(H_2O)]^-$ by ultra-filtration through a 5 kDA cutoff membrane and revealed that for a 150-300

μM [Mn(PyC3A)(H_2O)]$^-$ solution, 1-5% is protein bound in both plasma and 4.5% w/v BSA solutions.

[Mn(PyC3A)(H_2O)]$^-$ is an effective MRI contrast agent with rapid renal and hepatic clearance in mice

Key criteria in the development of a Gd-alternative are 1) extracellular distribution, 2) rapid clearance, and 3) mixed renal and hepatic elimination. We used dynamic MRI to assess these criteria in mice. Figures 2A-C show a series of coronal MR images prior to, 3, and 25 min following intravenous administration of 60 μmol/kg Na[Mn(PyC3A)(H_2O)]. After initial blood pool enhancement, the compound is rapidly cleared from the blood. Elimination occurs through the kidneys and into the bladder, but also through the liver. We drew regions of interest (ROIs) on the left ventricle of the heart (blood), the liver, and kidney, and measured the change in normalized signal to noise ratio (nSNR) as a function of time. Figures 2D-F depict normalized signal to noise ratio (nSNR) for the blood, kidney, and liver. The nSNR vs time curves were fit to a monoexponential for each animal to obtain a half-life for the probe in that tissue, and then the mean half-life was calculated using the data from the 4 animals. The kinetics of blood clearance, $t_{1/2}$ = 7.8±3.0 min, is similar to small Gd-based chelates in mice. These imaging studies demonstrate that [Mn(PyC3A)(H_2O)]$^-$ provides good image contrast, has the expected extracellular distribution, and is rapidly cleared via a mixed renal/ hepatic pathway. Mn tissue content was determined by ICP-MS 24h following probe injection (N=4) and compared against endogenous Mn levels recorded in naïve mice (N=4) (Figure 3). At 24h, <0.05% injected dose per gram of tissue (%ID/g) remains in the liver and kidneys while Mn levels in all other tissues are not elevated above endogenous basal levels.

Design and synthesis of fibrin-targeting probe Mn-FBP

Encouraged by the favorable relaxivity and stability profile of [Mn(PyC3A)(H_2O]$^-$, we sought to directly apply the complex to a targeted molecular imaging application. We chose fibrin, a principal component of thrombus (blood clot), as our molecular target. Fibrin is an insoluble polymeric protein network that forms following vascular insult via protease action of thrombin on the serum constituent protein fibrinogen. Enzymatic crosslinking fortifies the fibrin network. Fibrin is present at >10 μM concentration in thrombi and thus represents a sufficiently abundant target for molecular MR imaging.[22] Molecular imaging of fibrin could be used to detect the culprit lesion or source embolus in various thromboembolic diseases such as heart attack, stroke, deep vein thrombosis, or pulmonary embolism.

We used a short cyclic peptide shown to have high selectivity for fibrin over serum proteins.[49-51] This peptide was previously modified to enhance fibrin affinity and conjugated to imaging reporters (PET, MR, optical) for fibrin imaging in animal models of thrombosis and cancer.[52-56] A highly optimized Gd-based derivative, EP-2104R, was used to detect thrombi in humans.[57,58] We sought to develop a conjugate similar to EP-2104R using [Mn(PyC3A)(H_2O]$^-$ in order to compare how the Mn-chelate compared to Gd in a well established molecular probe.

The pyridyl moiety provides an easy and achiral means to incorporate additional functionality at a position remote from the Mn ion. The 5-position was substituted to prepare the bi-functional chelate ^{t}Bu-PyC3A-NHS (Scheme 2). Coupling of **5** (prepared in 2 steps) to **3** was followed by LiOH hydrolysis of the nicotinoyl methyl ester to yield **7**; subsequent NHS activation yielded the *O*-protected, bi-functional chelate. 4 mol equiv. ^{t}Bu-PyC3A-NHS were coupled to the tetra-amine functionalized peptide,[51] to yield **8** (Figure S7). *O*-deprotection of **8** yielded the tetrameric peptide-chelate conjugate **9** (Figure S7). Mn-FBP was prepared by stirring **9** with $MnCl_2$ at pH 6.5. EP-2104 shares the same structure as Mn-FBP except the 4 Mn-chelates are replaced by 4 $[Gd(DOTAGA)(H_2O)]^-$ chelates (Figure S7).

Mn-FBP is a high relaxivity probe with high affinity to fibrin

The per Mn relaxivity of Mn-FBP is increased 4-fold compared to $[Mn(PyC3A)(H_2O)]^-$ (r_1 = 8.5 vs 2.1 $mM^{-1}s^{-1}$, respectively), owing to the larger size and slower rotational diffusion [59] of the peptide-chelate conjugate, Figure 4A. Relaxivity is unchanged when measured in human fibrinogen solution, but increases to 13.5 $mM^{-1}s^{-1}$ when the fibrinogen is converted to a fibrin gel. This 60% increase in relaxivity in the presence of fibrin is expected due to further slowing of rotation upon binding and is similar to what is observed with EP2104R, Figure S13.[51] The lack of relaxivity increase in fibrinogen suggests no binding to this protein. There is an intermediate increase in relaxivity when measured in bovine blood plasma (10.7 $mM^{-1}s^{-1}$) or BSA solution (11.4 $mM^{-1}s^{-1}$) suggesting some weak interaction with albumin. The molecular relaxivity of Mn-FBP is 4-fold higher than the per Mn values and this high relaxivity is required for in vivo thrombus imaging.

We measured the affinity of Mn-FBP to the soluble fibrin fragment DD(E), by measuring the displacement of a fluorescent peptide from this protein (Figure 4B, fluorescent peptide in Figure S7).[49] Mn-FBP showed nanomolar affinity for DD(E), K_d = 110 nM compared to a K_d = 240 nM for EP-2104R measured with the same DD(E) preparation.

Variable temperature ^{17}O NMR indicated that Mn-FBP is q=1 with $k_{ex} = 1.1 \times 10^8$ s^{-1} (Figure S14, Table 2). Clearly the $[Mn(PyC3A)(H_2O)]^-$ solution structure and water exchange dynamics are negligibly effected by conjugation to the larger peptide structure, and its high relaxivity properties are maintained.

Mn-FBP detects arterial thrombus

We used a clinical 1.5T MR scanner to compare the ability of Mn-FBP to detect carotid artery thrombosis in a rat model with that of EP-2104R. A thrombus was generated in the right carotid artery by application of $AlCl_3$ solution to the vessel wall. A flow deficit at the site of injury was identified by time-of-flight (TOF) MR angiography (Figure S15). Thrombus formation was further confirmed by histology. For thrombus detection we used a 3D T_1-weighted gradient echo sequence with arterial inflow suppression. Imaging was performed prior to- and immediately following femoral artery injection of 10 μmol/kg Mn-FBP or EP-2104R (40 μmol/kg Mn or Gd). Scanning was repeated for a period of 1h post injection to assess the dynamics of thrombus uptake (N=4 per probe).

Figure 5A shows an axial T_1-weighted image taken before Mn-FBP injection. The region containing the carotid arteries is expanded in Figure 5C and the presence of thrombus cannot be observed in this image. Figures 5B and 5D show the same image slice 35 minutes after Mn-FBP injection where there is strong signal enhancement in the injured carotid but no enhancement in the contralateral vessel. Histological staining confirming thrombosis at the site of enhancement is shown in Figure 5E. Sagittal images depicting the extent of the thrombus are shown in Figure S16.

We quantified the imaging by measuring nSNR for thrombus, contralateral vessel and muscle as a function of time (Figure 5F). Probe accumulation in the thrombus is readily apparent by an 80% increase in nSNR. Our positive control, EP-2104R also showed strong thrombus enhancement (Figure 5G) with a peak nSNR increase that is smaller than, but not statistically different than the increase with Mn-FBP. We also calculated the contrast-to-noise ratio (CNR) between thrombus and muscle and between contralateral vessel and muscle as a function of time for Mn-FBP and EP-2104R, Figure 5H and 5I, respectively. For Mn-FBP, thrombus-to-muscle CNR increased more than 5-fold post injection and remained high through the course of the study. Thrombi were highly conspicuous with CNR reaching a plateau by 35 minutes post Mn-FBP with peak CNR vs. muscle = 32.9±4.0 vs. 5.6±1.5 for the thrombus vs. contralateral vessel, respectively (P=0.0001).

EP-2104R also identified the thrombi with high conspicuity, Figure 5I, and the peak thrombus-to-muscle CNR was smaller than, but not statistically different than for Mn-FBP. Sample images acquired using EP2104R are shown in Figure S17. On the other hand, thrombi were not readily identifiable in the baseline scans; thrombus-to-muscle vs. contralateral vessel-to-muscle CNR = 6.0±5.2 vs. 3.5±2.4, respectively (N=8, P=0.23).

Mn-FBP is eliminated intact after injection

We measured the biodistribution of Mn-FBP in rats at 1.5 and 24h post injection by Mn ICP-MS, Figure 6A,B. To account for endogenous Mn, we also measured the organ distribution of Mn in naïve rats. Most of the Mn-FBP (90±3%) was excreted into the urine by 1.5h. Figure 6A displays nmol recovered Mn or Gd per gram tissue at 1.5h after intravenous injection of Mn-FBP, EP2104R, and $MnCl_2$ (all dosed at 40 μmol metal ion per kg body weight). The distributions of Mn and Gd are very similar at 1.5h; unchelated Mn^{2+} distributes very differently and is highly accumulated in tissues such as the heart, liver and bone. Like EP2104R, Mn-FBP is largely cleared by 1.5h, with a little Mn remaining in the kidneys (1.7±0.2 %ID/g). In Figure 6B we show the concentration of Mn in different tissues 24h after Mn-FBP injection and the endogenous Mn concentrations found in naïve rats. At 24h almost all of the Mn is eliminated with <0.5% ID/g in the kidneys. The only tissues with significantly higher Mn concentrations than basal levels are the kidneys and muscle at this time point.

The Mn blood pharmacokinetics were analyzed by ICP-MS using blood drawn between 0 and 24h following probe injection. Figure 6D depicts the mean blood Mn concentrations from the 4 animals as a function of time. Total Mn blood clearance ($t_{1/2}$ = 22.6±6.8 min, calculated from biexponential fits to the individual animal data) mirrors the probe clearance

kinetics observed with other molecular imaging probes derived from the same fibrin binding peptide [54].

We also analyzed Mn speciation in blood plasma. This was performed using HPLC coupled ICP-MS for Mn detection. The Mn chromatograms revealed no evidence of Mn dechelation (Figure 6C). Two species are present in blood plasma, Mn-FBP ($t_{1/2}$ = 23.5±13.4 min, Figure 6E) and a small, unidentified Mn-FBP degradation product that also clears over the course of the study (Figure 6F). This degradation product also arises after in vitro plasma incubation of Mn-FBP but is not identified after incubation with $MnCl_2$ (Figure S18). Thus, the new species does not correspond to free Mn^{2+} or any Mn-containing species that arise after Mn dechelation. The HPLC-ICP-MS experiments suggest negligible concentrations of species arising from dechelated Mn.

Discussion

Our investigation demonstrates that a rationally designed Mn^{2+}-based imaging probe can achieve high relaxivity without undergoing significant in vivo dissociation. The $[Mn(PyC3A)(H_2O)]^-$ complex has plasma relaxivity comparable to clinically used Gd-based contrast agents, and is one of the most thermodynamically stable and kinetically inert Mn^{2+} complexes with respect to Mn dechelation. In mice, the complex is rapidly eliminated from the body via mixed renal and hepatic pathways and less than 1% of the injected dose remains in the body at 24 hours after injection. The $[Mn(PyC3A)(H_2O)]^-$ complex can be easily modified to incorporate into targeted molecular imaging probes without loss of stability or relaxivity. Indeed, the biophysical strategies used to enhance relaxivity in Gd complexes all apply to divalent Mn as well. The fibrin targeted probe Mn-FBP was prepared with enhanced relaxivity owing to an optimization of the rotational correlation time relative to the simple chelate, fast water exchange, and multimerization. In vivo, Mn-FBP was functionally equivalent to the state of the art Gd fibrin probe EP-2104R. Using a clinical MRI scanner, we could easily detect arterial blood clots as regions of bright signal after Mn-FBP injection. Importantly, Mn-FBP was rapidly and completely eliminated from the body in a largely unchanged state. While some probe metabolism was observed, it was not related to dechelated Mn. These findings support the use of $[Mn(PyC3A)(H_2O)]^-$ and its derivatives as alternatives to Gd-based contrast agents.

Gadolinium-based contrast agents are entrenched in clinical radiology. Over half of the MRI procedures at our institution employ a Gd-based contrast agent. Several factors feature in their success: the compounds are extremely safe in their intended population; they provide positive signal change that is easy to interpret; diagnostic images can be obtained shortly after injection. The major limitation of Gd-based contrast agents is their risk in the renally impaired patient population. Mn-based imaging probes represent the most broadly feasible method solution to provide contrast-enhanced images in patients contraindicated for iodinated CT contrast and/or Gd. Discrete Mn^{2+} complexes also produce positive image contrast, have similar pharmacokinetic and pharmacodynamic behavior to analogous Gd-complexes, and can be prepared as hydrophilic complexes with low non-specific protein binding. Mn^{2+} relaxation enhancement is similar in magnitude to Gd-based complexes, and thus the effective dose is similar between Mn and Gd. A key difference between Mn^{2+} and

Gd^{3+} is the distribution of the free ion. If there is some dechelation of Mn, there is an efficient, endogenous elimination pathway through the hepatobiliary system. Such a path does not exist for Gd and accumulation and toxicity can occur.

Alternate contrast enhancing approaches have limitations with respect to replacing Gd. Paramagnetic nanoparticles have unfavorable pharmacokinetics that limit their use to blood vessel or liver imaging, or require a long delay after injection for target accumulation and/or background clearance. Probes detected via CEST or direct nuclear observation require an order of magnitude higher dose than Gd or Mn which raises toxicity concerns, especially in a renally compromised population. Hyperpolarized techniques require expensive changes in hardware and the need for an onsite polarizer; Mn probes on the other hand are shelf stable.

The longstanding challenge for Mn^{2+} probes is the instability and high lability of the complexes. High spin Mn^{2+} has no ligand field stabilization energy to reduce metal ion lability, and Mn^{2+} is at the low end of the Irving-Williams series with respect to thermodynamic stability. For MR applications, an inner-sphere water ligand is required and this results in sacrificing a donor group in the multidentate ligand designed to chelate the Mn. The PyC3A chelator is a hexadentate ligand that forms a 7-coordinate ternary complex with Mn^{2+}, leaving a site for water to coordinate. The *trans*-cyclohexylene backbone provides preorganization to enhance both stability and inertness, while the pyridyl moiety improves inertness relative to an acetate donor group. Remarkably, the complex is more inert to Zn transmetallation than $[Gd(DTPA)(H_2O)]^{2-}$. Overall, this combination of stability and inertness is sufficient to maintain in vivo fidelity. The cyclohexylene and pyridyl components of $[Mn(PyC3A)(H_2O)]^-$ provide a modest lipophilicity to the anionic complex which promotes some hepatic uptake and elimination.

We hypothesize that $[Mn(PyC3A)(H_2O)]^-$ and its derivatives can be effective replacements for Gd-based contrast agents, especially in populations where Gd usage carries additional risk. The Mn-FBP studies indicate the stability of the Mn-chelate in vivo. In a patient with low GFR where the Mn-chelate may circulate longer, we expect that any slowly released Mn^{2+} will be eliminated through the liver. We note that $Mn[DPDP]^{3-}$ was safely used in thousands of patients and this complex is extremely unstable with respect to Mn^{2+} dechelation ($[Mn(PyC3A)(H_2O)]^-$ is $>10^5$ times more stable than $[Mn(DPDP)]^{3-}$ at pH 7.4).

A limitation of our study is that we did not formally address the toxicity of $[Mn(PyC3A)(H_2O)]^-$ and Mn-FBP, nor study their in vivo behavior in a model of chronic kidney disease. The goal of the current work was to design a better chelator for Mn^{2+} and to establish that the resultant complex is stable in vivo and enables elimination of Mn. Formal studies of the safety and efficacy of these compounds in models of renal disease are planned. However we note that our imaging and biodistribution studies in rats showed no signs of acute toxicity.

Conclusion

Rationally designed $[Mn(PyC3A)(H_2O)]^-$ achieves the optimal balance of thermodynamic stability, kinetic inertness and high relaxivity demanded of a MR imaging probe. The probe provides excellent MR contrast and is rapidly and completely eliminated from the body via

renal and hepatic pathways. $[Mn(PyC3A)(H_2O)]^-$ lends nicely to synthetic modulation, and we prepared a bifunctional derivative for bioconjugation. The fibrin-targeted conjugate Mn-FBP, provides strong enhancement of carotid artery thrombosis with conspicuity equivalent to the state of the art Gd-based probe EP-2104R. Mn-FBP is highly stable with respect to Mn dechelation in vivo and promotes whole body Mn clearance. The combined results of our physicochemical, MR imaging, and pharmacokinetics experiments indicate that $[Mn(PyC3A)(H_2O)]^-$, both on its own and as a bifunctional synthon, is a lead candidate for developing non-Gd MR imaging probes.

Supplementary Material

Refer to Web version on PubMed Central for supplementary material.

Acknowledgments

Funding Source: This work was supported by grants from the National Cancer Institute (T32CA009502 to E.M.G, R01CA161221 to P.C.) and the National Institute for Biomedical Imaging and Bioengineering (R01EB009062 to P.C.) and instrumentation funded by the National Center for Research Resources and the Office of the Director (RR14075, OD010650). I.P.A was supported by a fellowship from the Comunidad de Madrid and the Madrid MIT M+Vision Consortium.

References

1. United States Renal Data System. 2014 USRDS annual data report: An overview of the epidemiology of kidney disease in the United States. National Institutes of Health, National Institute of Diabetes, Digestive and Kidney Diseases; 2014.
2. Gullion CM, Keith DS, Nichols GA, Smith DH. Am J Kidney Dis. 2006; 48:212. [PubMed: 16860186]
3. Shastri S, Samak MJ. Am J Kidney Dis. 2010; 56:399. [PubMed: 20599309]
4. Hage FG, Venkataraman R, Zoghbi GJ, Perry GJ, DeMattos AM, Iskandrian AE. J Am Coll Cardiol. 2009; 53:2129. [PubMed: 19497438]
5. Coresh J, Selvin E, Stevens LA, Manzi J, Kusek JW, Eggers P, Van Lente F, Levy AS. J Am Med Assoc. 2007; 298:2038.
6. Nash K, Hafeez A, Hou S. Am J Kidney Dis. 2002; 39:930. [PubMed: 11979336]
7. Solomon RJ, Natarajan MK, Doucet S, Sharma SK, Staniloae CS, Katholi RE, Gelormini JL, Labinaz M, Moreyra AE. Circulation. 2007; 115:3189. [PubMed: 17562951]
8. Grobner T. Nephrol Dial Transplant. 2006; 21:1104. [PubMed: 16431890]
9. Marckmann P, Skov L, Rossen K, Dupont A, Damholt MB, Heaf JG, Thomsen HS. J Am Soc Nephrol. 2006; 17:2359. [PubMed: 16885403]
10. Yang L, Krefting I, Gorovets A, Marzella L, Kaiser J, Boucher R, Rieves D. Radiology. 2012; 265:248. [PubMed: 22923714]
11. ACR Manual on Contrast Media v10 1. American College of Radiology; U.S.A: 2015.
12. Besheli LD, Aran S, Shaqdan K, Kay J, Abujudeh H. Clinic Radiol. 2014; 69:661.
13. Kanda T, Fukusato T, Matsuda M, Toyoda K, Oba H, Kotoku J, Haruyama T, Kitajima K, Furui S. Radiology. 2015; 276:228. [PubMed: 25942417]
14. Kanda T, Osawa M, Oba H, Toyoda K, Kotoku J, Haruyama T. Radiology. 2015; 275:803. [PubMed: 25633504]
15. Kanda T, ishii K, Kawaguchi H, Kitajima K, Takenaka D. Radiology. 2014; 270:834. [PubMed: 24475844]
16. Kanda T, Kawaguchi H. Neuroradiology. 2013; 55:1268.
17. McDonald RJ, McDonald JS, Kallmes DF, Jentoft ME, Murray DL, Thielen KR, WIlliamson EE, Eckel LJ. Radiology. 2015; 275:772. [PubMed: 25742194]

18. Kanal E, Tweedle MF. Radiology. 2015; 275:630. [PubMed: 25942418]
19. Bashir MR, Bhatti L, Marin D, Nelson RC. J Magn Res Imag. 2015; 41:884.
20. [March 30, 2015] FDA Orders Stricter Warnings for Ferumoxytol (Feraheme). Medscape. 2015. onlinehttp://www.medscape.com/viewarticle/842309
21. Aime S, Castelli DD, Geninatti S, Gianolio E, Terreno E. Acc Chem Res. 2009; 42:822. [PubMed: 19534516]
22. Boros E, Gale EM, Caravan P. Dalton Trans. 2015; 44:4804. [PubMed: 25376893]
23. Lauffer RB. Chem Rev. 1987; 87:901.
24. Hamm B, Vogl TJ, Branding G, Schnell B, Taupitz M, Woft KJ, LIssner J. Radiology. 1992; 182:167. [PubMed: 1309218]
25. Vogl TJ, Hamm B, Schnell B, McMahon C, Branding G, LIssner J, Wolf KJ. J Magn Res Imag. 1993; 3:51.
26. Gallez B, Bacic G, Swartz HM. Magn Reson Med. 1996; 35:14. [PubMed: 8771018]
27. Ni Y, Petré C, Bosmans H, Miao Y, Grant D, Baert AL, Marchal G. Acta Radiolog. 1997; 38:700.
28. Chandra T, Pukenas B, Mohan S, Melhem E. Magn Reson Imaging Clin N Am. 2012; 20:687. [PubMed: 23088945]
29. Leiner T, Michaely H. Magn Reson Imaging Clin N Am. 2008; 16:561. [PubMed: 18926422]
30. Moon M, Cornfield D, Weinreb J. Magn Reson Imaging Clin N Am. 2009:2.
31. Essig M, Dinkel J, Gutierrez JE. Magn Reson Imaging Clin N Am. 2012; 20:633. [PubMed: 23088943]
32. Keston P, Murray AD, Jackson A. Clin Radiology. 2003; 58:505.
33. Kálmán FK, Tircsó G. Inorg Chem. 2012; 51:10065. [PubMed: 22974437]
34. Gale EM, Mukherjee S, Liu C, Loving GS, Caravan P. Inorg Chem. 2014; 53:10748. [PubMed: 25226090]
35. Caravan P, Ellison JJ, McMurry TJ, Lauffer RB. Chem Rev. 1999; 99:2293. [PubMed: 11749483]
36. Aime S, Anelli PL, Botta M, Brocchetta M, Canton S, Fedeli F, Gianolio E, Terreno E. J Biol Inorg Chem. 2002; 7:58. [PubMed: 11862541]
37. Troughton JS, Greenfield MT, Greenwood JM, Dumas S, Wiethoff AJ, Wang J, Spiller M, McMurry TJ, Caravan P. Inorg Chem. 2004; 43:6313. [PubMed: 15446878]
38. Maigut J, Meier R, Zahl A, van Eldik R. Inorg Chem. 2008; 47:5702. [PubMed: 18510310]
39. Drahoš B, Lukeš I, Tóth E. Eur J Inorg Chem. 2012; 2012:1975.
40. Caravan P, Rettig SJ, Orvig C. Inorg Chem. 1997; 36:1306. [PubMed: 11669706]
41. Caravan P, Farrar CT, Frullano L, Uppal R. Contrast Media Mol Imag. 2009:89.
42. Drahoš B, Kubíček V, Bonnet CS, Hermann P, Lukeš I, Tóth E. Dalton Trans. 2011; 40:1945. [PubMed: 21274464]
43. Drahoš B, Pniok M, Havlíčková J, Kotek J, Císařová I, Hermann P, Lukeš I, Tóth E. Dalton Trans. 2011; 30:10131. [PubMed: 21887440]
44. Drahoš B, Kotek J, Císařová I, Hermann P, Helm L, Lukeš I, Tóth E. Inorg Chem. 2011; 50:12785. [PubMed: 22092039]
45. Drahoš B, Kotek J, Hermann P, Lukeš I, Tóth E. Inorg Chem. 2010; 49:3224. [PubMed: 20180546]
46. Gale EM, Zhu J, Caravan P. J Am Chem Soc. 2013; 135:18600. [PubMed: 24088013]
47. Caravan P, Parigi G, Chasse JM, Cloutier NJ, Ellison JJ, Lauffer RB, Luchinat C, McDermid SA, Spiller M, McMurry TJ. Inorg Chem. 2007; 46:6632. [PubMed: 17625839]
48. Rohrer M, Bauer H, Mintorovitch J, Requardt M, Weinmann HJ. Invest Radiol. 2005; 40:715. [PubMed: 16230904]
49. Kolodziej AF, Nair SA, Graham P, McMurry TJ, Ladner RC, Wescott C, Sexton DJ, Caravan P. Bioconjugate Chem. 2012; 23:548.
50. Kolodziej AF, Zhang Z, Overoye-Chan K, Jacques V, Caravan P. Methods Mol Biol. 2014; 1088:185. [PubMed: 24146405]

51. Overoye-Chan K, Koerner S, Looby RJ, Kolodziej AF, Zech SG, Deng Q, Chasse JM, McMurry TJ, Caravan P. J Am Chem Soc. 2008; 130:6025. [PubMed: 18393503]
52. Uppal R, Medarova Z, Farrar CT, Dai G, Moore A, Caravan P. Invest Radiol. 2012; 47:553. [PubMed: 22960948]
53. Uppal R, Catana C, Ay I, Benner T, Sorenson AG, Caravan P. Radiology. 2011; 258:812. [PubMed: 21177389]
54. Blasi F, Oliveria BL, Rietz TA, Rotile NJ, Day H, Looby RJ, Ay I, Caravan PJ. Nucl Med. 2014; 55:1157.
55. Ay I, Blasi F, Rietz TA, Rotile NJ, Kura S, Brownell AL, Day H, Oliveria BL, Looby RJ, Caravan P. Circ Cardiovasc Imaging. 2014; 7:697. [PubMed: 24777937]
56. Ciesienski KL, Yang Y, Ay I, Chonde DB, Loving GS, Rietz TA, Catana C, Caravan P. Mol Pharmaceutics. 2013; 56:1782.
57. Vymazal J, Spuentrup E, Cardenas-Molina G, Wiethoff AJ, Hartmann MG, Caravan P, Parsons EC Jr. Invest Radiol. 2009; 44:697. [PubMed: 19809344]
58. Spuentrup E, Botnar RM, Wiethoff AJ, Ibrahim T, Kelle S, Katoh M, Ozgun M, Nagel E, Vymazal J, Graham PB, Günther RW, Maintz D. Eur Radiol. 2008; 18:1995. [PubMed: 18425519]
59. Zhou X, Caravan P, Clarkson RB, Westlund PO. J Magn Reson. 2004; 167:147. [PubMed: 14987609]

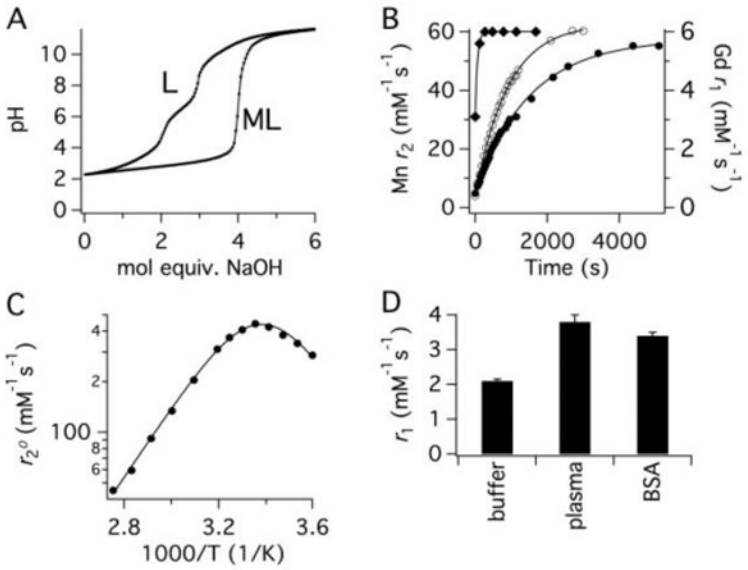

Figure 1.

(A) pH titration of PyC3A•TFA in the absence (L) and presence (ML) of 1 equiv $MnCl_2$ at 25 °C, I = 0.15 M NaCl. (B) Transmetallation of 1 mM $[Gd(DTPA)(H_2O)]^{2-}$ (filled diamonds), $[Mn(CDTA)(H_2O)]^{2-}$ (open circles) or $[Mn(PyC3A)(H_2O)]^{-}$ filled circles) by 25 mM Zn^{2+} monitored by relaxivity change as a function of time in 50 mM pH 6.0 MES buffer, 37 °C, 1.4T. (C) $H_2{}^{17}O$ tranverse relaxivity in the presence of $[Mn(PyC3A)(H_2O)]^{-}$ as a function of temperature. Solid lines are fits to the data. (D) r_1 of $[Mn(PyC3A)(H_2O)]^{-}$ measured in pH 7.4 Tris buffer, bovine blood plasma, and 4.5% wt/v bovine serum albumin (BSA) at 1.4T, 37 C°.

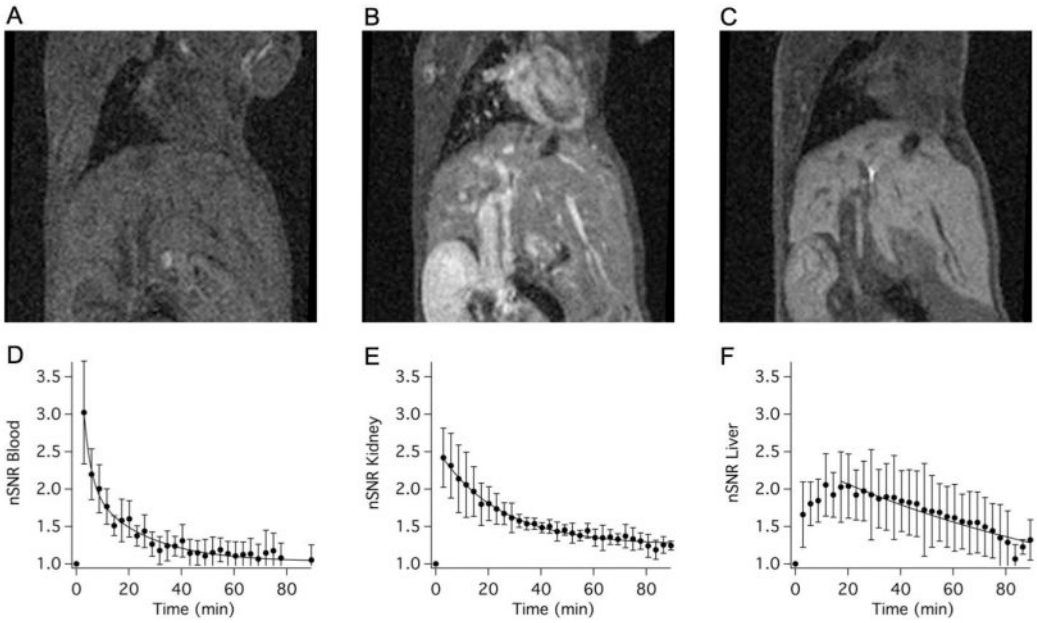

Figure 2.

Coronal T_1-weighted MR images of a balb/C mouse acquired prior to (A), 3 min (B), and 25 min (C) following i.v. administration of 60 μmol/kg $Na[Mn(PyC3A)(H_2O)]^-$. Normalized signal-to-noise ratio (nSNR) as a function of time in the blood (D), kidney (E), and liver (F) following $Na[Mn(PyC3A)(H_2O)]^-$ injection; N=4, error bars represent standard error of the mean; solid lines are monoexponential fits to the mean data.

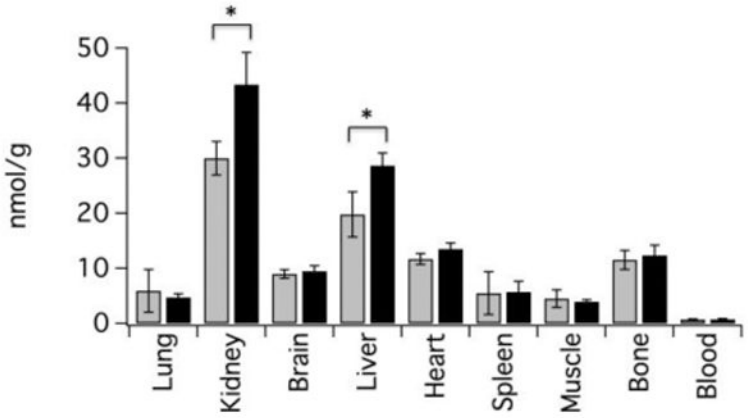

Figure 3.

Endogenous Mn concentration (nmol/g) in mouse tissues (grey bars, N=4, determined from naïve mice) and Mn tissue levels 24h following intravenous injection of 60 μmol/kg Na[Mn(PyC3A)(H_2O)] (black bars, N=4). Statistically elevated Mn levels (*, $P<0.05$) were observed only in the kidney and liver and together represent <0.05% of the injected dose per gram tissue.

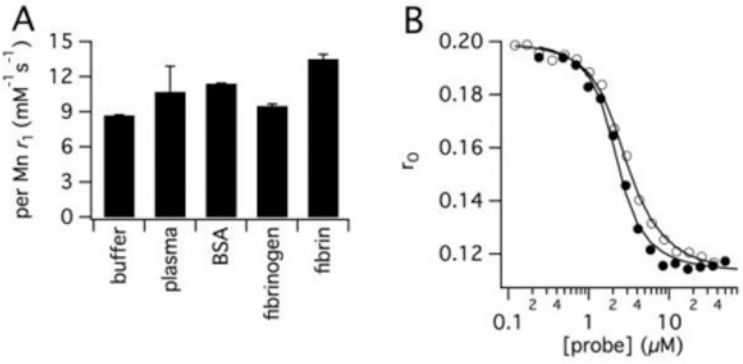

Figure 4.

(A) r_1 of Mn-FBP measured in pH 7.4 Tris buffer, bovine blood plasma, 4.5% wt/v BSA, human fibrinogen and human fibrin gel at 1.4T, 37 C°. The 60% r_1 increase in the presence of fibrin gel is the result of the reduction in Mn-FBP tumbling rate upon protein binding. (B) Fluorescence polarization anisotropy of fluorescein labeled fibrin binding peptide in DD(E) solution as a function of added Mn-FBP (filled circles) or EP2104R (open circles) to determine Ki to DD(E).

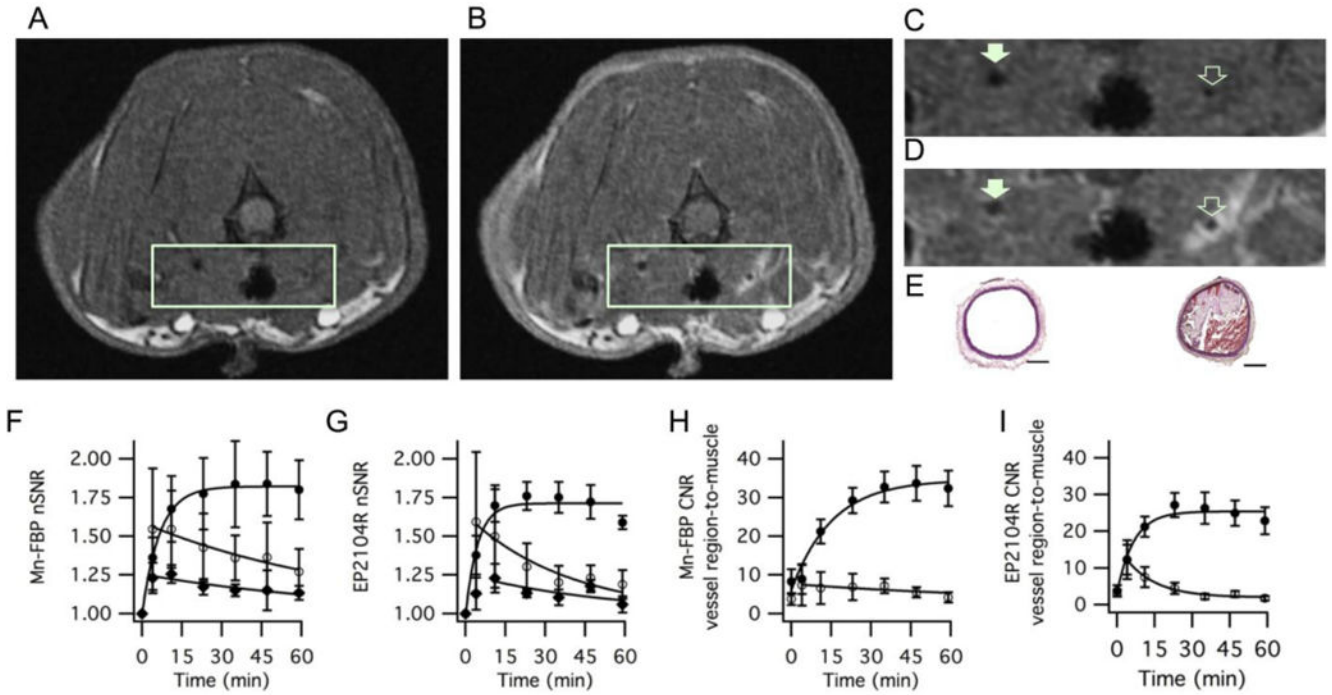

Figure 5.

Molecular MR imaging of carotid artery thrombus in a rat model with Mn-FBP. Axial T_1-weighted images before (A, C) and 35 minutes after intravenous administration of Mn-FBP (B, D) at 1.5T. (C) and (D) are expanded regions from (A) and (B), respectively showing the common carotid arteries. Mn-FBP generates marked signal enhancement in the ipsilateral vessel (open arrow, D) after Mn-FBP injection, but not in contralateral vessel (filled arrow, D) or in the vessel prior to Mn-FBP injection (C). (E) Hematoxylin and Eosin stained sections of contralateral (left) and ipsilateral (right) carotid arteries showing occlusive thrombus in the injured vessel; scale bar = 300 μm. (F) and (G) show normalized signal-to-noise ratio (nSNR) of the thrombus (closed circles), contralateral vessel region (open circles), and muscle (closed diamonds) following administration of Mn-FBP and EP2104R, respectively, showing persistently enhanced thrombus with each probe and washout of signal from background tissue. (H) and (I) contrast-to-noise ratio (CNR) of thrombus-to-muscle (closed circles) and contralateral vessel region-to-muscle (open circles) following administration of Mn-FBP and EP2104R, respectively, showing large and persistently high CNR for the thrombus with each probe . N=4 for each probe, error bars represent standard error of the mean.

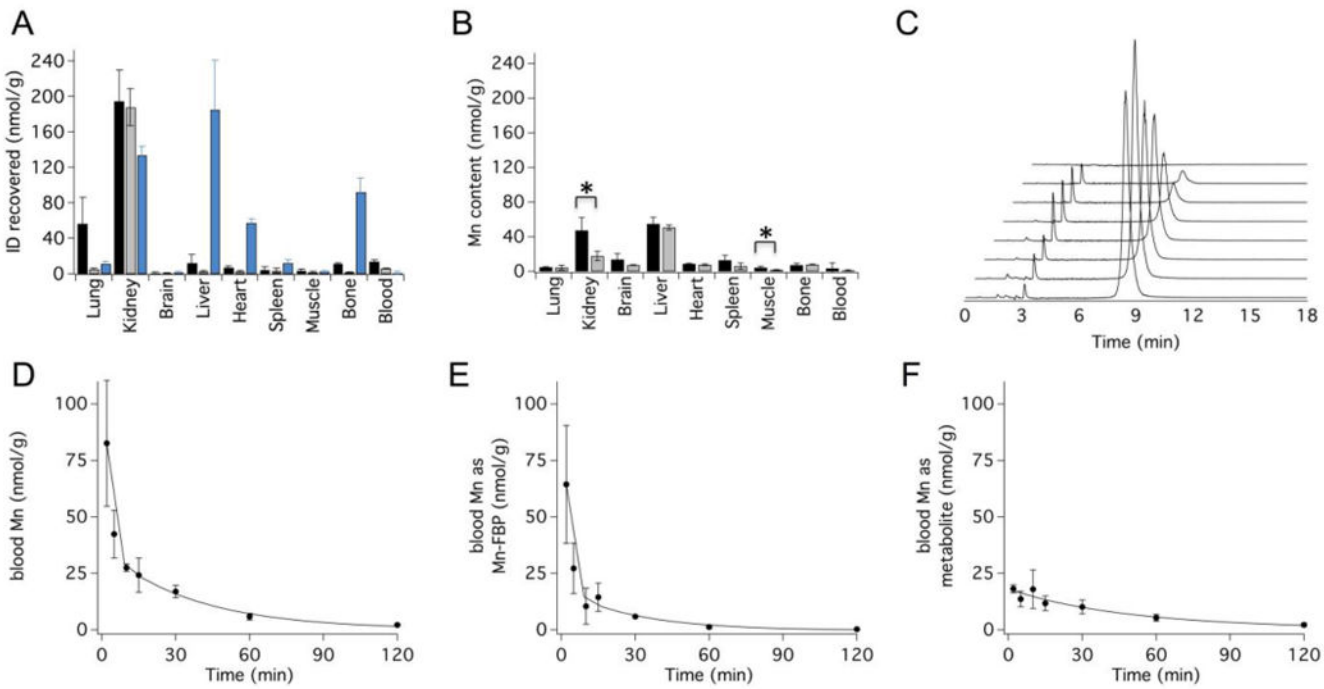

Figure 6.

(A) Concentration of Mn or Gd in rat tissues (nmol metal per g tissue) 1.5h after intravenous administration of 40 μmol metal ion per kg body weight of Mn-FBP (black bars), EP2104R (grey bars), and $MnCl_2$ (blue bars); Mn levels are corrected for endogenous baseline metal content, N=4 per probe. (B) Concentration (nmol/g) of Mn in rat tissues at 24h following Mn-FBP administration (black bars, N=4) or in naïve rats (grey bars, N=4, showing endogenous Mn levels). Statistically significant differences (*, $P<0.05$) were observed in kidney and muscle and represent 0.37±0.14 and 0.02±0.02 percent of the injected dose per gram tissue, respectively. (C) LC-ICP-MS traces of plasma analyzed for Mn from blood drawn 2 min, 5 min, 15 min, 30 min, 1h, 2h, and 24h (front to back) after intraveneous Mn-FBP injection. Mn-FBP elutes at 8.5 min; no species arising from dechelated Mn are detected in the LC-ICP-MS traces. (D-F) Pharmacokinetic data (N=4) showing blood clearance of total Mn (D), Mn-FBP (E), and the metabolite eluting at 3.1 min (F), demonstrating rapid blood elimination of Mn-FBP and its metabolite. Error bars represent standard error of the mean; solid lines are biexponential fits to the mean data.

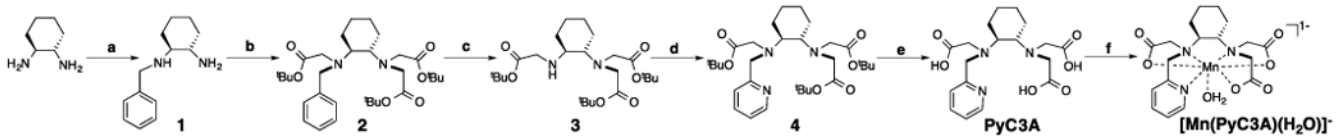

Scheme 1.

Synthesis of $[Mn(PyC3A)(H_2O)]^-$ (a) substoicheometric benzyl bromide, dioxane, RT; (b) 3 equiv. ^{t}butyl-bromoacetate, 1 equiv. KI, DIPEA, DMF, RT; (c) 1 atm H_2 (g), 10% by wt. Pd/C, MeOH; (d) picolyl chloride, KI, DIPEA, DMF, RT; (e) 1:1 CH_2Cl_2:TFA, RT; (f) $MnCl_2$, pH 6.5.

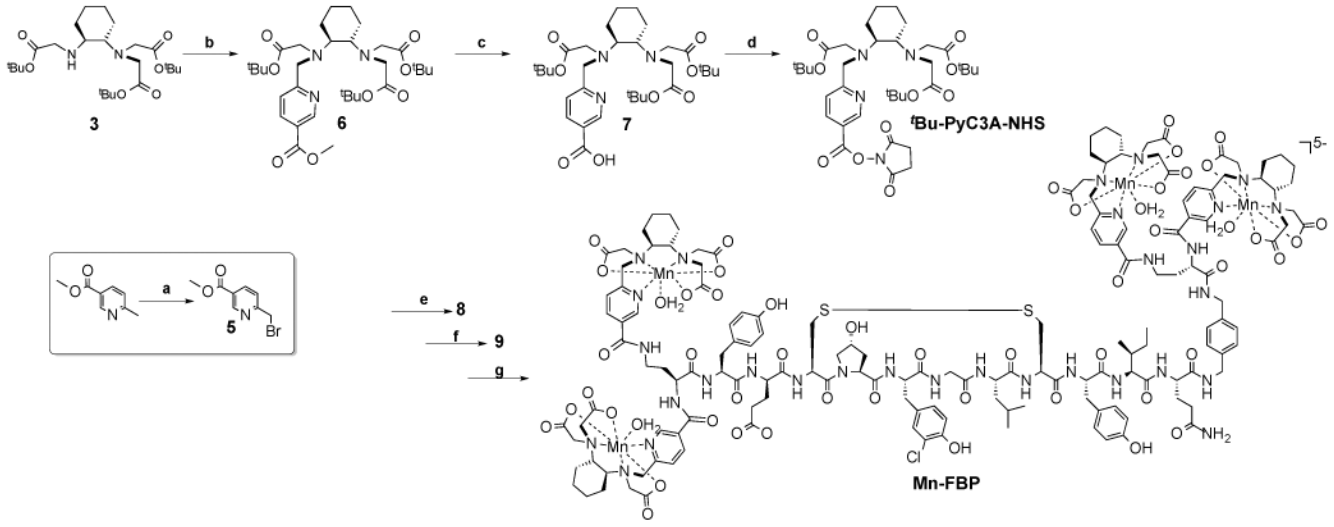

Scheme 2.

Synthesis of Mn-FBP. (a) N-bromosuccinimide, cat. benzoyl peroxide, CCl_4, reflux; (b) 5, KI, DIPEA, DMF, RT; (c) LiOH, 1:1 THF:H_2O, RT; (d) N,N′,-dicyclohexylcarbodiimine, N-hydroxysucciminide, THF, RT; (e) tetra-amine functionalized fibrin binding peptide, cat. DMAP, DIPEA, DMF, RT; (f) 91:3:3:3 TFA:methanesulfonic acid:1-dodecanethiol:H_2O, RT; (g) $MnCl_2$, pH 6.5. The structures of **8** and **9** are shown in Figure S7.

Table 1

Protonation[a] and formation[b] constants of ligands and their corresponding Mn(II) complexes

	$logK_{LH}$	$logK_{LH2}$	$logK_{LH3}$	$logK_{LH4}$	$logK_{ML}$	$logK_{MLH}$	$logK_{pH\ 7.4}$[c]	pMn (pH 7.4)[d]
PyC3A	10.16±0.02	6.39±0.04	3.13±0.03	--	14.14±0.01	2.43±0.03	11.34, 11.40±0.13[e]	8.17, 8.20[e]
EDTA	9.17,[33] 9.35[34]	5.99[33] 5.98[34]	2.73,[33] 2.48[34]	2.01,[33] 2.23[34]	12.46,[33] 12.61[34]	2.95,[33] 2.90[34]	10.49,[33] 10.67[34]	7.82,[33] 7.83
CDTA	9.36,[33] 9.43[34]	5.95,[33] 6.01[34]	3.62,[33] 3.68[34]	2.57,[33] 2.51[34]	14.32,[33] 14.69[34]	2.90,[33] 2.42[34]	12.34,[33] 12.64[34]	8.67,[33] 8.82

[a] Values were obtained by pH-potentiometry (25 °C, I = 0.15 M NaCl). K_{LHn} defined as $[H_nL]/([H][H_{n-1}L])$.

[b] K_{ML} defined as [ML]/([M][L]); K_{HML} defined as [HML]/([ML][H]) (charges omitted for clarity).

[c] Effective formation constant at pH 7.4.

[d] pMn defined as –log[free Mn] when [M] = [L] = 10 μM.

[e] Value obtained from K_{comp} determined using CDTA challenge.

Table 2

Hydration state (*q*), water exchange parameters and $Mn^{-17}O$ hyperfine coupling constant ($A_O/\hbar$) of corresponding Mn(II) complexes

	q	k_{ex}^{310} ($\times 10^8$ s^{-1})	$\Delta H^{\neq}$ (kJ/mol)	$A_O/\hbar$ ($\times 10^7$ rad/s)
$[Mn(PyC3A)]^-$	1	1.0±0.02	37.2	2.87±0.080
Mn-FBP	1	1.1±0.04	39.7	2.82±0.040